Journal of Materials Chemistry C

ROYAL SOCIETY OF CHEMISTRY

PAPER

View Article Online
View Journal | View Issue

Cite this: J. Mater. Chem. C, 2021, 9, 14916

Spin structures and band gap reduction of high-pressure triple perovskite $Mn_3MnTa_2O_9$†

Elena Solana-Madruga, *[a] Clemens Ritter,[b] Olivier Mentré [a] and Ángel M. Arévalo-López *[a]

Received 6th September 2021,
Accepted 7th October 2021

DOI: 10.1039/d1tc04231a

rsc.li/materials-c

Herein we report the second transition-metal-only triple perovskite $Mn_3MnTa_2O_9$, from high pressure-high temperature transformation of $Mn_4Ta_2O_9$. It shows 1:2 Mn:Ta B-site order and a complex antiferromagnetic behavior with a collinear structure that modulates into a spin density wave. The high pressure phase presents a 25% band gap reduction compared to its multiferroic precursor, recoverable above 625 °C.

Introduction

The flexibility of transition metal (TM) perovskite oxides (ABO_3, Pv) allows accommodation of a wide variety of elements into both A and B sites and thus tuning of their promising technological applications.[1,2] Different types of cation ordered derivatives can also be obtained and their physical properties enhanced, for instance Sr_2FeMoO_6 (double perovskite DPv, 1:1 B-site ordering), where the Fe–Mo cation order promotes its room temperature colossal magnetoresistance.[3] Exotic perovskites with small TM ions at the A-sites are usually stabilized under high-pressure, as in $CaCu_3Fe_2Re_2O_{12}$ (quadruple perovskite QPv with 1:3 A and 1:1 B site ordering).[4]

The growing family of A-site manganites is under intensive study, since the stabilization of Mn into the A-site in the perovskite structure *via* high-pressure (HP) provides a rich playground of potential spin, orbital and charge orders. Among them, simple (Pv, only $MnVO_3$),[5] double (DPv, *e.g.* Mn_2FeReO_6),[6] doubly ordered (also known as double DDPv, *e.g.* $MnRMnSbO_6$ with R = rare earth),[7] quadruple (QPv, *e.g.* $MnMn_3Mn_4O_{12}$)[8,9] and only very recently triple (TPv, only $Mn_3MnNb_2O_9$ with 1:2 B site ordering)[10] perovskite phases have been reported.

In the present study we prepared at high pressure and temperature $Mn_3MnTa_2O_9$, the second transition-metal-only $A_3BB'_2O_9$ triple perovskite, from the room pressure (RP) magnetoelectric $Mn_4Ta_2O_9$ at 8 GPa and 1100 °C. A comparative study with the closely related HP-$Mn_3MnNb_2O_9$ is presented here. Both isostructural compounds have a complex magnetic behavior, with three subsequent transitions at T_N = 52 K, T_M = 30.5 K and T_L = 6 K for Ta (52.1, 27.8 and 4.8 K respectively for the Nb compound), where Mn^{2+} spins order into a collinear antiferromagnetic (AFM) structure that modulates into a spin density wave (SDW) and locks-in at lower temperature as revealed by neutron powder diffraction (NPD). The band gap as measured from UV-vis and calculated from DFT for the new HP-$Mn_3MnTa_2O_9$ shows a reduction of 25% when compared to its room pressure precursor and we argue that this is due to the change in connectivity between both polymorphs offering a promising approach to adjust to ideal values for photovoltaic applications.

Results and discussion

Structural characterization was performed from the Rietveld fit against high resolution NPD data (λ = 1.54 Å, collected on D20 @ ILL). Fig. 1a shows the structural features of the TPv model refined using Full Prof suite[11] and summarized in Table 1. HP-$Mn_3MnTa_2O_9$ crystallizes with the acentric monoclinic *Cc* symmetry with a = 9.8992(3) Å, b = 5.3267(2) Å, c = 13.2472(5) Å and β = 92.736(3)° cell parameters. As for HP-$Mn_3MnNb_2O_9$,[10] the *C*2/*c* symmetry was tested and found in worse agreement (ESI†), the superstructure peaks (200), (002) and (110) support the refined *Cc* model (ESI† Fig. SF1). The refined structure shows perfect 1:2 cation order between Mn^{2+} (Mn_2, blue) and Ta^{5+} (Ta_1 and Ta_2, orange) among the B sites (being isostructural to HP-$Mn_3MnNb_2O_9$), see Fig. 1b. Mn–O distances up to 3.5 Å confirm octahedral coordination for Mn2, with all bond lengths between 1.99 Å and 2.28 Å. Otherwise, Mn1 (black), Mn3 (red) and Mn4 (green) show 12-, 11- and 10-fold coordination respectively, according to their location

[a] Univ. Lille, CNRS, Centrale Lille, ENSCL, Univ. Artois, UMR 8181 – UCCS – Unité de Catalyse et Chimie du Solide, F-59000 Lille, France.
E-mail: elena.solanamadruga@univ-lille.fr, angel.arevalo-lopez@univ-lille.fr
[b] Institut Laue-Langevin, Avenue des Martyrs 71, 32042, Grenoble Cedex, France

† Electronic supplementary information (ESI) available: Supporting figures and tables. See DOI: 10.1039/d1tc04231a

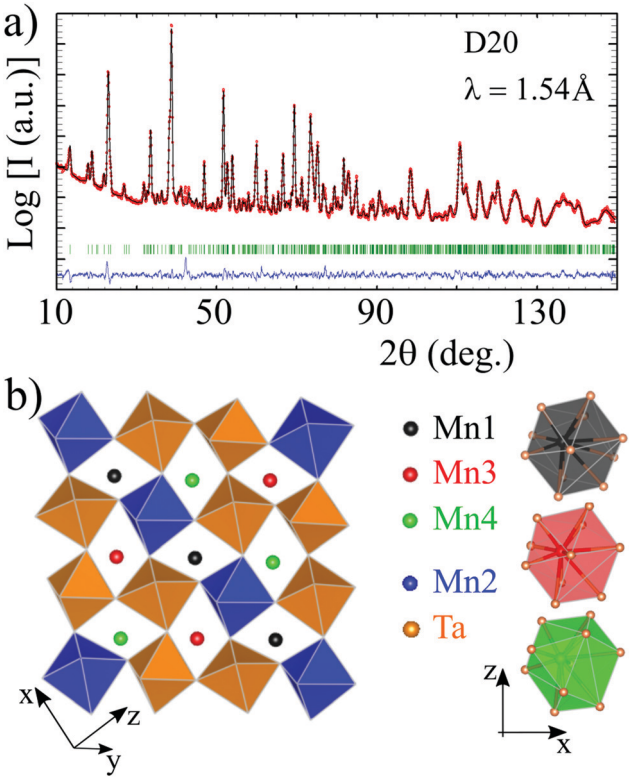

Fig. 1 (a) Rietveld fit against 300 K high resolution NPD data of HP-$Mn_3MnTa_2O_9$. (b) Refined TPv crystal structure. One (11-2) plane with the B-site order of Mn2 and Ta is shown on the left panel and 12-, 11- and 10-fold coordination polyhedra of Mn A sites on the right panel.

Table 1 Atomic positions (all Wyckoff 4a sites fully occupied) of HP-$Mn_3MnTa_2O_9$ refined from the 300 K high resolution NPD data. Space group *Cc* and cell parameters a = 9.8992(3) Å, b = 5.3267(2) Å, c = 13.2472(5) Å and β = 92.736(3)°. Thermal parameters constrained for cations and anions refine to 0.53 (5) and 0.54(2) Å^2 respectively

Site	x	y	z
Mn1	0.728(2)	0.494(4)	0.428(1)
Mn2	0.440(3)	0.479(3)	0.476(2)
Mn3[a]	0.394	0.5	0.757
Mn4	0.551(2)	−0.012(4)	0.589(1)
Ta1	0.105(1)	0.508(3)	0.823(1)
Ta2	0.770(1)	0.511(2)	0.652(1)
O1	0.724(2)	0.698(2)	0.776(1)
O2	0.194(1)	0.687(2)	0.697(1)
O3	0.111(1)	0.864(3)	0.070(1)
O4	0.853(1)	0.337(2)	0.538(1)
O5	0.514(1)	0.688(2)	0.367(1)
O6	0.563(1)	0.186(2)	0.449(1)
O7	0.767(1)	0.864(3)	0.395(1)
O8	0.450(2)	0.885(1)	0.744(1)
O9	0.387(1)	0.294(2)	0.624(1)

	Mn1	Mn2	Mn3	Mn4	Ta1	Ta2
$\langle\lambda\rangle$	1.086	1.016	1.089	1.060	1.009	1.012
$10^3\Delta$	10.4	37.7	5.6	8.1	4.1	3.8
σ^2 (deg^2)	254.2	46.5	266.2	182.6	20.7	31.3
BVS	1.94	2.45	2.03	2.07	4.67	4.71

[a] Mn3 site used as a cell reference.

into A sites of the TPv structure. The structural distortion parameters, including $a^-b^-c^-$ tilt angles (Φ_1 = 18.90°, Φ_2 = 23.20° and Φ_3 = 24.25°) and polyhedral distortions (quadratic elongation and bond angle variance, see Table 1) are of the same order of magnitude as those observed for the related HP-$Mn_3MnNb_2O_9$ TPv.[10] This suggests that A-site manganites with 1 : 2 B-site order could generally stabilize much greater distortions with respect to Pv, DPv and QPv materials (SF2, ESI†). Bond Valence Sum (BVS) calculations confirm nominal Mn^{2+} and Ta^{5+} oxidation states, with compensated mismatches among the B-site cations reflecting the strain in the structure and the necessity to stabilize it at high pressure.

A comparative study of the crystal structures of HP-$Mn_3MnB'_2O_9$ with B′ = Ta and Nb (see Table 2) indicates their main differences concern coordination numbers of MnA sites and tilt angles. Higher A-site coordination is found for B′ = Ta, supporting the perovskite-related structure. Smaller Φ_1 and Φ_2 while larger Φ_3 values compared with those in HP-$Mn_3MnNb_2O_9$, agree with the relative lattice parameters, two of which are longer for HP-$Mn_3MnTa_2O_9$. Similar unit cell volumes reflect the close synthesis conditions for both compounds, coherently with their equivalent ionic radii (0.64 Å for both Nb^{5+} and Ta^{5+}).[12] This is also reflected in similar global distortion parameters which confirms their close stability, suggesting other related high pressure compounds should be accessible from HPHT phase transition from the $A_4B_2O_9$ niobates and tantalates first reported by Bertaut *et al.*[13] Consequently, new complex HP-TPv are currently under study.

Magnetic susceptibility data (top panel in Fig. 2) show two clear magnetic transitions at T_N = 52 K and T_M = 30.5 K. These transitions are also observed as λ peaks in heat capacity measurements (see SF2, ESI† for derivative curves and T_N and T_M assignment). A low temperature anomaly (T_L = 6 K) is assigned to a lock-in transition of the modulated magnetic phase, in accordance to NPD results as described below (Fig. 2 middle and bottom panels). Curie–Weiss fit to the inverse susceptibility above 150 K results in an effective magnetic moment of 6.0(1) μ_B/Mn^{2+}, in good agreement with the expected value of 5.92 μ_B/Mn^{2+}, and θ = −237(1) K, suggesting dominant AFM interactions with strong magnetic frustration ($f = |\theta|/T_N$ = 4.6(1). A similar behavior was observed for HP-$Mn_3MnNb_2O_9$, the main difference between both compounds being the clear lambda-like transition observed in the Nb compound at T_L. Here, this lock-in is more evident from NPD data (*vide infra*) while the derivative of heat capacity data (SF2, ESI†) shows a broad maximum.

Table 2 Compared main structural features of HP-$Mn_3MnB'_2O_9$ (B′ = Nb, Ta)

B′	Nb	Ta
MnA coordination	10, 10, 8	12, 11, 10
Φ_1, Φ_2, Φ_3 (°)	20, 25, 16	19, 23, 24
a (Å)	9.9054(5)	9.8992(3)
b (Å)	5.3097(2)	5.3267(2)
c (Å)	13.2052(7)	13.2472(5)
β (°)	92.772(6)	92.736(3)
V (Å^3)	693.72(3)	697.73(5)

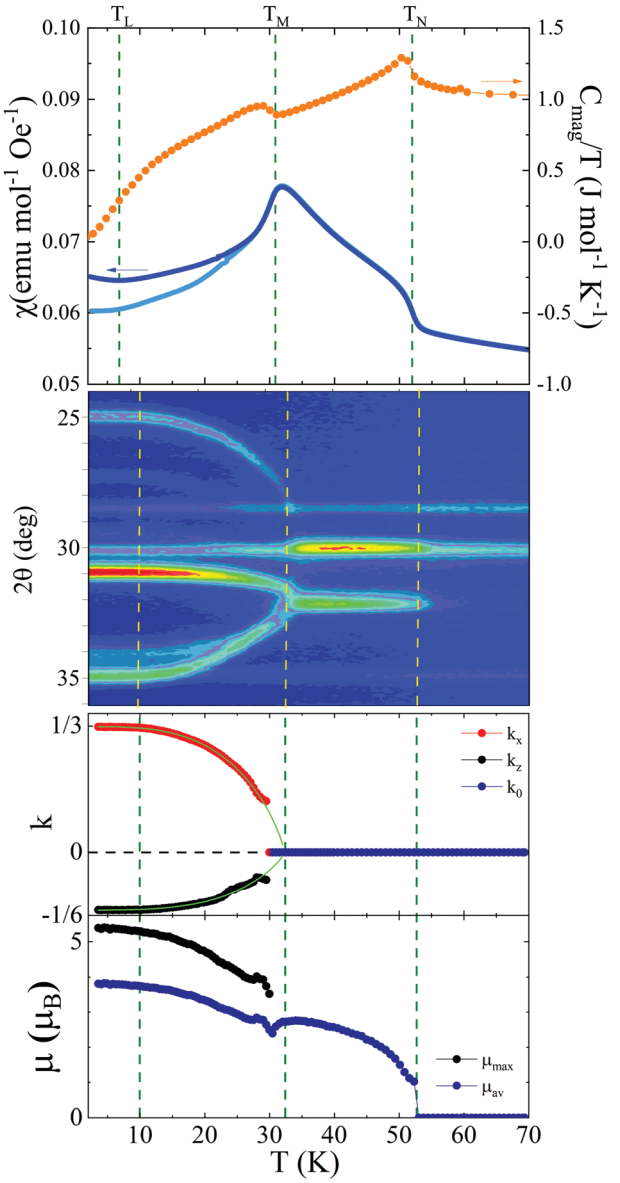

Fig. 2 Temperature dependence of magnetic susceptibility and heat capacity (top panel), neutron diffraction (middle) and refined propagation vector and magnetic moment (bottom). Dashed lines mark T_N, T_M and T_L transition temperatures. Green lines in bottom panel show the fit of k vectors to a critical law. μ_{max} stand for maximum values in the SDW phase and μ_{av} for averaged ($\mu/2\pi$) magnetic moments.

The thermal evolution of NPD data (λ = 2.41 Å, D20@ILL) focused on the 24–36° 2θ region is depicted in the middle panel of Fig. 2. These data confirm that HP-$Mn_3MnTa_2O_9$ undergoes an AFM transition below 54 K, marked with a dashed line. A coherent increase of the intensity of these magnetic peaks is observed down to 32 K (both T_M and T_N show a 2 K difference respect to bulk properties, usual from experimental details), where the magnetic susceptibility describes a maximum, and a sharp transition occurs, involving the immediate shift of the magnetic peaks. All magnetic peaks in the $T_N > T > T_M$ temperature range can be indexed with the propagation vector

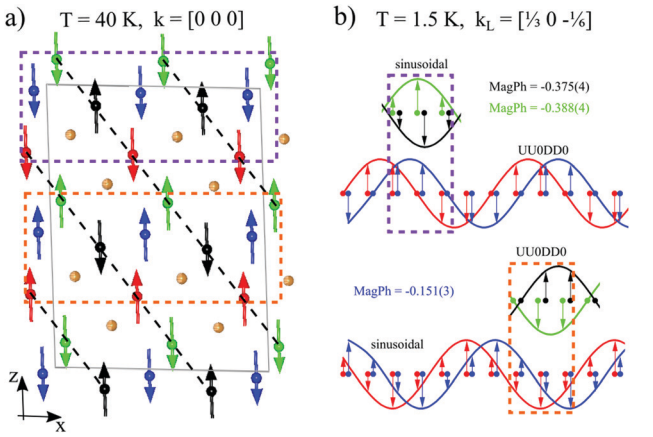

Fig. 3 (a) Magnetic structure of HP-$Mn_3MnTa_2O_9$ at 40 K with k_0 = [0 0 0]. AFM (101) MnA planes (red–green–black) are highlighted with black dashed lines. Orange spheres represent Ta sites and the dashed purple and orange boxes highlight sections of the nuclear cell with different sine patterns at low temperature. (b) Schematic representation of UU0DD0 and sinusoidal waves at 1.5 K with k_L = [1/3 0 −1/6], where Mn2 (blue)/Mn3 (red) and Mn1 (black)/Mn4 (green) waves with closer propagation are coupled for simplicity. A single unit is shown for Mn1/Mn4 sites while longer sections are shown for Mn2/Mn3. Magnetic phase factors (relative shifts of the waves) are indicated.

k_0 = [0 0 0], where it develops a collinear magnetic structure with all magnetic moments along the easy c axis. This magnetic structure refined from NPD data collected at 40 K is shown in Fig. 3a. It describes AFM (101) planes of MnA sites (black dashed lines). MnB (blue) sites align AFM with Mn1 (black), according to dominant direct d^5–d^5 interactions through octahedral face sharing.[14] The need for FM interactions between MnB and Mn3 (red)/Mn4 (green) A sites induces magnetic frustration. Below T_M, the magnetic frustration of MnB sites (*vide infra*), induces a sinusoidal modulation of the magnetic moments into a complex SDW magnetic structure with k_M = [k_x 0 k_z]. This modulation involves the continuous evolution of the propagation vector towards k_x = 1/3 and k_z = −1/6, where they are locked below 10 K (Fig. 2 bottom panel). Averaged magnetic moments (μ_{av} = $\mu/2\pi$) evolve progressively throughout the complete temperature range, reaching a maximum value of 3.81(1) μ_B. This value corresponds to 76.2% of the ideal 2S = 5 value for Mn^{2+}, in line with the change in magnetic entropy estimated from heat capacity (see ESI†).

The low temperature magnetic structure, schematized in Fig. 3b, can be described as a SDW with k_L = [1/3 0 −1/6] and magnetic moments modulated along the c easy axis, varying between zero and saturated values of 5.1 (1) μ_B. Two different types of sine waves propagating along the a axis alternate along c, showing up–up-0-down–down-0 (UU0DD0) and 3up–3down (sinusoidal) patterns. Similarly complex frustrated magnetic structures are reported in the only oxynitride A-site manganite with Ta, $MnTaO_2N$.[15] The magnetic frustration between A and B sites is the driving force for the modulation of these unusual SDW in A-site manganites with TPv structure (see below and ESI† for details).

The most distinctive point of both TPv HP-$Mn_3MnB'_2O_9$ phases (B′ = Ta and Nb) is their magnetic frustration. While the Nb compound showed a larger frustration index (6.42), its collinear k_0 phase was dominant down to lower T_M = 27.8 K. As a result, the magnetic moment of Mn^{2+} spins increased in this k_0 phase for HP-$Mn_3MnNb_2O_9$ to maximum values of 2.68(1) μ_B before modulating into the SDW, while the Ta compound reported here reaches only 2.50(1) μ_B in the collinear phase. The reason for the earlier modulation of the magnetic moments in HP-$Mn_3MnTa_2O_9$ compared to the Nb analogue is the larger constraint function,[16] *i.e.* the energy ratio between the ground SDW and the hypothetical non-modulated collinear phases. The energy of both magnetic phases can be estimated using a classical spin description as $E_f(k_0) = \Sigma J_{ij}{*}s_i{*}s_j$, where J_{ij} is the spin exchange parameter and s_i and s_j are the magnetic moments of i and j sites. Considering a hypothetical AFM non-modulated phase at low temperature with all equivalent (μ_{av}) magnetic moments 2.50 μ_B, $E_f(k_0)$ = 1350*J. The spin modulation minimizes the number of frustrated (FM MnB–MnA) interactions in the k_L phase, which decrease from 12 to 5 in each unit cell (see SF4, ESI†). Therefore, accounting for the 18 cells per magnetic cell and the different magnetic moments in the UU0DD0 waves (4.33 μ_B) and in the sinusoidal waves (5 or 2.5 μ_B), the estimated $E_f(k_L)$ = 1177.2*J. The ratio $F = E_f(k_0)/E_f(k_L)$ = 1.15, suggests maximum values of 2.2 μ_B/Mn^{2+} would be reached in the hypothetical non-modulated structure to keep the same energy, while the modulation of the magnetic moments allows their partial saturation with averaged moments near 80% of their ideal value. Therefore, the magnetic frustration between A and B sites is confirmed to be the driving force for the modulation of these unusual SDW in A-site manganites with TPv structure. A similar estimation for HP-$Mn_3MnNb_2O_9$ results in F = 1.32, thus showing a larger frustration.

High temperature XRD studies revealed the reversibility of the structural phase transition back to the room pressure polymorph $Mn_4Ta_2O_9$ upon heating HP-$Mn_3MnTa_2O_9$ at room pressure. As shown in Fig. 4a, it is a first order transition starting at 625 °C and completed at 780 °C. A comparison between both structures is presented in Fig. 4a. The corner-sharing B-site scaffold for the HP TPv phase is highlighted (blue $MnBO_6$ and orange TaO_6 octahedra). Compared with $Mn_4Ta_2O_9$, the main structural difference is the antiphase rotation between the TaO_6 octahedra ending up in the characteristic face sharing in the room pressure polymorph. These changes in connectivity have a strong effect in the optical properties.

Kubelka–Munk plots of our experimental UV-vis reflectance spectra (Fig. 4b) show a ΔE_{gap} = 0.9 eV from the $Mn_4Ta_2O_9$ precursor (E_{gap} = 3.5 eV) to the $Mn_3MnTa_2O_9$ TPv high pressure phase (E_{gap} = 2.6 eV). DFT+U (U = 5 eV) calculations in a ferromagnetic configuration were performed for both polymorphs (Fig. 4c). A E_{gap} = 2.4 eV was obtained for RP-$Mn_4Ta_2O_9$ in accordance with previous reports.[17] HP-$Mn_3MnTa_2O_9$ shows a reduced E_{gap} = 1.5 eV. Although both calculated gaps are underestimated by ≈1 eV from their

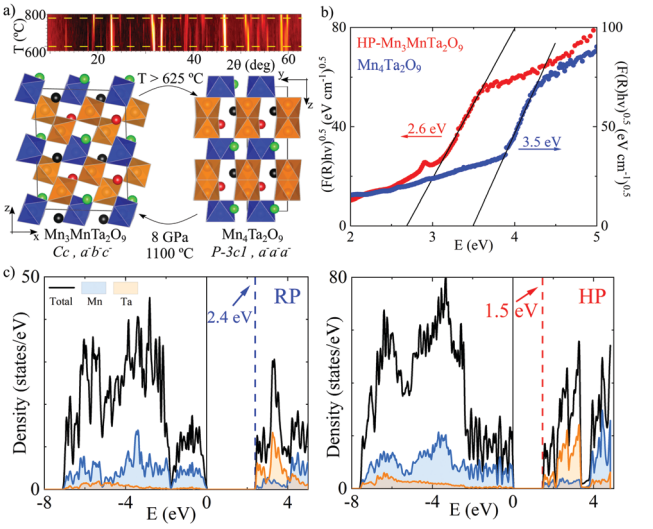

Fig. 4 (a) XRD thermodiffraction patterns showing a room pressure phase transition from the *Cc* TPv structure of HP-$Mn_3MnTa_2O_9$ to the $P\bar{3}c1$ structure of $Mn_4Ta_2O_9$. The transition temperature range (625–780 °C) is delimited with dashed lines. Projections along [010] of HP-$Mn_3MnTa_2O_9$ (left) and [100] of $Mn_4Ta_2O_9$ (right) structures compared below. (b) UV-Vis data showing 25% band gap reduction. (c) Density of states calculated for the room (left) and high-pressure (right) polymorphs.

experimental values, they show the same ΔE = 0.9 eV gap shift. Moreover, the E_{gap} reduction in $Mn_3MnTa_2O_9$ is mainly due to the Ta octahedra, lying at the bottom of the conduction band that shows a red shift. This is commonly related to the change in connectivity between both polymorphs, the denser being prone to easier carrier hopping. The most critical structural reorganization involves the collapsing of face-sharing electron-blocking Ta_2O_9 dimers ($d_{(Ta-Ta)}$ = 3.08 Å) and edge-sharing Ta–Mn links ($d_{(Ta-Mn)}$ = 3.17 Å) in the RP form, for face sharing Mn–Ta bridges ($d_{(Mn-Ta)}$ = 3.03 Å) in the HP-polymorph, more prompt to delocalization. Mn_3TeO_6 also shows a similar reduction in the band gap between the room (E_{gap} = 2.6 eV) and the high-pressure polymorphs (E_{gap} = 1.8 eV).[18] The differences between both structures in Mn_3TeO_6 are also due to a drastic structural reorganization of the polyhedral connectivity. A similar explanation has been found for the gap variation between light-harvesting lead iodide perovskite-derived compounds.[19] In the case of the here discussed modifications of RP-$Mn_4Ta_2O_9$ and HP-$Mn_3MnTa_2O_9$, the gap reduction is mainly promoted by the change in the TaO_6 octahedra connectivity.

Conclusions

In conclusion a new HP-$Mn_3MnTa_2O_9$ A-site manganite with TPv structure and 1:2 B-site order of Mn and Ta has been prepared under HPHT conditions. This is notable as it represents only the second transition-metal-only compound ever reported to show this *Cc* structure, suggesting a new complete family of functional oxides is accessible. The complex magnetic behavior arises from highly frustrated Mn–Mn interactions

giving rise to an unusual SDW with propagation vector $k = [1/3\ 0\ -1/6]$ locked at low temperatures, dictated by the B-site cation order and reflecting the key role of the triangular antiferromagnetic sublattices. The metastable HP-$Mn_3MnTa_2O_9$ TPv polymorph transforms back into the ambient $Mn_4Ta_2O_9$ structure above 625 °C. The connectivity changes between the room- and the high-pressure polymorph promotes a band gap reduction as observed in UV-vis measurements and further confirmed by DFT calculations.

Author contributions

The study was designed by A. M. A. L. Synthesis was performed by E. S. M. Bulk magnetism and heat capacity data were measured and analyzed by E. S. M. and A. M. A. L. Neutron diffraction data were collected and analyzed by E. S. M., A. M. A. L. and C. R. DFT calculations were performed by O. M. The paper was written by E. S. M. and A. M. A. L. with collaborations from all authors.

Conflicts of interest

There are no conflicts to declare.

Acknowledgements

We thank support from ANR AMANTS project (19-CE08-0002-01) and the ILL for beamtime at D20 (doi: 10.5291/ILL-DATA.EASY-858) The Chevreul Institute (FR 2638), Region Hauts-de-France, and FEDER are acknowledged for funding the X-ray diffractometers, the "LEGO" multianvil-press and the PPMS magnetometer.

Notes and references

1 S. Vasala and M. Karppinen, *Prog. Solid State Chem.*, 2015, **43**, 1–36.
2 A. T. Mulder, N. A. Benedek, J. M. Rondinelli and C. J. Fennie, *Adv. Funct. Mater.*, 2013, **23**, 4810–4820.
3 K.-I. Kobayashi, T. Kimura, H. Sawada, K. Terakura and Y. Tokura, *Nature*, 1998, **395**, 677–680.
4 W.-t. Chen, M. Mizumaki, H. Seki, M. S. Senn, T. Saito, D. Kan, J. P. Attfield and Y. Shimakawa, *Nat. Commun.*, 2014, **5**, 3909.
5 M. Markkula, A. M. Arévalo-López, A. Kusmartseva, J. A. Rodgers, C. Ritter, H. Wu and J. P. Attfield, *Phys. Rev. B: Condens. Matter Mater. Phys.*, 2011, **84**, 094450.
6 A. M. Arévalo-López, G. M. McNally and J. P. Attfield, *Angew. Chem., Int. Ed.*, 2015, **54**, 12074–12077.
7 E. Solana-Madruga, A. M. Arévalo-López, A. J. Dos santos-García, E. Urones-Garrote, D. Ávila-Brande, R. Sáez-Puche and J. P. Attfield, *Angew. Chem., Int. Ed.*, 2016, **55**, 9340–9344.
8 S. V. Ovsyannikov, A. M. Abakumov, A. A. Tsirlin, W. Schnelle, R. Egoavil, J. Verbeeck, G. Van Tendeloo, K. V. Glazyrin, M. Hanfland and L. Dubrovinsky, *Angew. Chem., Int. Ed.*, 2013, **52**, 1494–1498.
9 D. D. Khalyavin, R. D. Johnson, P. Manuel, A. A. Tsirlin, A. M. Abakumov, D. P. Kozlenko, Y. Sun, L. Dubrovinsky and S. V. Ovsyannikov, *Phys. Rev. B*, 2018, **98**, 014426.
10 E. Solana-Madruga, C. Ritter, C. Aguilar-Maldonado, O. Mentré, J. P. Attfield and Á. M. Arévalo-López, *Chem. Commun.*, 2021, **57**, 8441–8444.
11 J. Rodriguez-Carvajal, *Phys. B*, 1993, **192**, 55–69.
12 R. D. Shannon and C. T. Prewitt, *Acta Crystallogr., Sect. B: Struct. Crystallogr. Cryst. Chem.*, 1969, **25**, 925–946.
13 E. F. Bertaut, L. Corliss and F. Forrat, *J. Phys. Chem. Solids*, 1961, **21**, 234–251.
14 J. B. Goodenough, *Magnetism and the Chemical Bond*, New Wiley, New York, 1963, pp. 180–181.
15 C. Tassel, Y. Kuno, Y. Goto, T. Yamamoto, C. M. Brown, J. Hester, K. Fujita, M. Higashi, R. Abe, K. Tanaka, Y. Kobayashi and H. Kageyama, *Angew. Chem., Int. Ed.*, 2015, **54**, 516–521.
16 D. Dai and M. H. Whangbo, *J. Chem. Phys.*, 2004, **121**, 672–680.
17 N. Narayanan, A. Senyshyn, D. Mikhailova, T. Faske, T. Lu, Z. Liu, B. Weise, H. Ehrenberg, R. A. Mole, W. D. Hutchison, H. Fuess, G. J. McIntyre, Y. Liu and D. Yu, *Phys. Rev. B*, 2018, **98**, 134438.
18 Á. M. Arévalo-López, E. Solana-Madruga, C. Aguilar-Maldonado, C. Ritter, O. Mentré and J. P. Attfield, *Chem. Commun.*, 2019, **55**, 14470–14473.
19 M. E. Kamminga, G. A. de Wijs, R. W. A. Havenith, G. R. Blake and T. T. M. Palstra, *Inorg. Chem.*, 2017, **56**, 8408–8414.

